ORIGINAL ARTICLE

Monitoring of intracerebral hemorrhage with a linear microwave imaging algorithm

İsmail Dilman[1] · Egemen Bilgin[2] · Mehmet Nuri Akıncı[1] · Sema Coşgun[3] · Semih Doğu[1] · Mehmet Çayören[1] ·
İbrahim Akduman[1]

Abstract

Intracerebral hemorrhage is a life-threatening condition where conventional imaging modalities such as CT and MRI are indispensable in diagnosing. Nevertheless, monitoring the evolution of intracerebral hemorrhage still poses a technological challenge. We consider continuous monitoring of intracerebral hemorrhage in this context and present a differential microwave imaging scheme based on a linearized inverse scattering. Our aim is to reconstruct non-anatomical maps that reveal the volumetric evolution of hemorrhage by using the differences between consecutive electric field measurements. This approach can potentially allow the monitoring of intracerebral hemorrhage in a real-time and cost-effective manner. Here, we devise an indicator function, which reveals the position, volumetric growth, and shrinkage of hemorrhage. Later, the method is numerically tested via a 3D anthropomorphic dielectric head model. Through several simulations performed for different locations of intracerebral hemorrhage, the indicator function-based technique is demonstrated to be capable of detecting the changes accurately. Finally, the robustness under noisy conditions is analyzed to assess the feasibility of the method. This analysis suggests that the method can be used to monitor the evolution of intracerebral hemorrhage in real-world scenarios.

Keywords Intracerebral hemorrhage · Microwave imaging · Inverse scattering

1 Introduction

Intracerebral hemorrhage (ICH) is a life-threatening emergency that can occur due to traumas and non-traumatic causes such as hypertension and arteriovenous malformations [1]. When an ICH diagnosis is admitted to the intensive care unit (ICU), the patient is regularly monitored with CT scans since increased intracranial pressure (due to bleeding) can damage the patient's brain tissues irreversibly. On the other hand, frequent exposure to ionizing radiation poses other dangers to the patient. Besides, in most hospitals, the patient is needed to be transported between ICU and radiology services, which may adversely affect the prognosis. Hence, continuous monitoring of the evolution of ICH poses a technological challenge in neurology. Microwave imaging (MWI) uses a non-ionizing electromagnetic spectrum with a relatively longer wavelength (in the order of centimeters). Due to longer wavelengths, the achievable resolutions are typically sub-optimal for medical imaging purposes. Nevertheless, envisioned potential benefits of such technology have long maintained a global research effort with diverse applications in medicine [2–7].

✉ İsmail Dilman
  dilman@itu.edu.tr

  Egemen Bilgin
  egemen.bilgin@mef.edu.tr

  Mehmet Nuri Akıncı
  akincime@itu.edu.tr

  Semih Doğu
  dogu16@itu.edu.tr

  Mehmet Çayören
  cayoren@itu.edu.tr

  İbrahim Akduman
  akduman@itu.edu.tr

[1] Dept. of Electronic and Communication Engineering, Istanbul Technical University, Maslak 34469, Istanbul, Turkey

[2] Dept. of Electrical and Electronics Engineering, MEF University, Maslak 34396, Istanbul, Turkey

[3] Dept. of Electrical and Electronic Engineering, Bolu Abant Izzet Baysal University, Gölköy 14030, Bolu, Turkey

In parallel to these efforts, microwave-based diagnosis and imaging technologies have been actively investigated for both hemorrhagic and ischemic strokes [8–20]. Due to critical conditions of ICH patients, experimental studies are restricted to the brain mimicking phantoms [21–27]. Hence, clinical performance of the technology is still an open question [28]. Among these diverse approaches, differential microwave imaging emerges as a promising technique for continuous monitoring of ICH [20, 22, 29]. In such techniques, the difference between consecutive electric field measurements of the brain is processed to determine the volumetric evolution of hemorrhage. Depending on the implemented imaging algorithm, such approaches can generate a map that reveals geometrical properties (location and shape) of hemorrhage without reconstructing the brain's anatomical images of the brain [22]. From an instrumentation perspective, a typical microwave imaging system does not require a dedicated facility (as in MRI or CT). In addition, such systems can be built compactly such that it can be possible to integrate them into the ambulances [30].

In this context, we considered monitoring ICH by differential microwave imaging and presented a new linear inversion algorithm, which takes both TM and TE polarizations into account to reveal the geometrical extent of ICH. Essentially, the human head is an inhomogeneous medium with a high degree of complex dielectric permittivity variations thus the weak scattering assumption for linearization (via Born approximation) does not hold. However, similar to other linear microwave imaging techniques [31–36], the reconstructed images can be evaluated qualitatively without determining the actual dielectric profile. Besides, as a consequence of electrochemical signaling among neurons, the brain has a relatively high electrical conductivity, which exponentially attenuates microwave exposure inside the brain. Hence, only microwave spectra with longer wavelengths can be effectively used, adversely affecting the resolution. In the ICH monitoring context, the field measurements at consecutive time steps are utilized to enhance the resolution. Therefore, the reconstructed images with the presented linear inversion algorithm correspond to the volumetric evolution of ICH. Furthermore, we propose an indicator function to clearly indicate the shrinkage or expansion of the hemorrhage. Later, the presented method is numerically verified by considering realistic constraints of microwave brain imaging, such as the requirements of the antenna array and the matching medium. With a set of simulations performed on an MRI-derived anthropomorphic head phantom [37], we further investigate the statistical robustness of the indicator function to determine the shrinkage or expansion of the hemorrhage. The demonstrated results indicate that the method is capable of accurately monitoring ICH even with noisy measurements.

2 Methods

Electromagnetic scattering by inhomogeneous dielectric mediums (such as the human brain) can be eloquently formulated with volumetric integral equations. When such integral equations are inverted to determine the dielectric profile by exploiting the measurements of scattered fields, the resulting formulations are inherently non-linear, and ill-posed [38]. Nevertheless, visualization of the reconstructed dielectric profile (or an associated quantity) corresponds to an image that has the potential to reveal the internal structure of the medium. In the following section, we formulate a linear microwave imaging technique that can accommodate both TM and TE polarizations.

2.1 TM polarization case

Let us consider that a patient's head is illuminated by a set of TM polarized time harmonic electromagnetic waves. Later, the scattered electric fields, which are due to electromagnetic interaction with the incident electromagnetic waves and the head, are measured as u_1^{sct} and u_2^{sct} for two consecutive time steps. The difference between these consecutive measurements can be represented with an integral equation

$$
\begin{aligned}
\Delta u_{TM}^{sct}(r) &= u_2^{sct}(r) - u_1^{sct}(r) \\
&= k_b^2 \int_{\Omega} g(r;r')\Delta\Omega(r')d\Omega(r')
\end{aligned}
\tag{1}
$$

over the volume of head Ω. Here $r \in S$ is the location of the receiving antenna, $r' \in \Omega$, and the Green's function with the wavenumber k_b of the surrounding medium is given by

$$
g(r,r') = \frac{i}{4} H_0^{(1)}(k_b|r - r'|).
\tag{2}
$$

where $H_0^{(1)}(.)$ is the zero-order Hankel function of the first kind. The term $\Delta\Omega(r')$ denotes the difference in the contrast source between two consecutive measurements. By assuming that the total electric field $U(r')$ inside the brain does not change significantly for these two consecutive measurements. The difference in the contrast source can be written as $\Delta\Omega(r') = \delta\chi(r')U(r')$, where $\delta\chi(r')$ denotes the variation of the dielectric contrast function. For differential imaging, the goal is to detect the changes in the contrast function ($\delta\chi(r')$), instead of the complete reconstruction of the contrast function $\chi(r')$ which is given by

$$
\chi(r') = k^2(r')/k_b^2 - 1.
\tag{3}
$$

By linearizing with Born approximation, Eq. (1) can be written as:

$$\Delta u_{TM}^{sct}(r) = k_b^2 \int_\Omega \delta\chi(r')g(r;r')U_e^{inc}(r')d\Omega(r') \qquad (4)$$

where U_e^{inc} is the incoming electric field for a line source:

$$U_e^{inc}(r') = \frac{i}{4}H_0^{(1)}(k_b|r - r'|) \qquad (5)$$

Later, Eq. (4) can be converted into a system of linear equations as:

$$\Delta u_{TM}^{sct} = A_{TM}\delta\chi \qquad (6)$$

where A_{TM} is the transformation matrix for TM case illumination. In order to determine the differential contrast function, Tikhonov regularization can be used as:

$$\delta\chi_{TM} = (A_{TM}^* A_{TM} + \alpha I)^{-1}A_{TM}^* u^{sct} \qquad (7)$$

where $\alpha > 0$ is the Tikhonov parameter and the superscript * denotes the adjoint operator [38].

2.2 TE polarization case

Let us again consider the same measurement scenario with TE polarized time harmonic electromagnetic waves to take advantage of measurements with TE polarizations. In this case, differential scattering electric field is a vector in the x-y plane and can be defined as:

$$\Delta u_{TE}^{sct}(r) = k_b^2 \int_\Omega \overline{\overline{G}}_{TE}(r;r')\Delta\Omega(r')d\Omega(r') \qquad (8)$$

where $\overline{\overline{G}}_{TE}$ is in the dyadic form and can be defined as:

$$\overline{\overline{G}}_{TE} = \begin{bmatrix} G_{xx} & G_{xy} \\ G_{yx} & G_{yy} \end{bmatrix} \qquad (9)$$

$$G_{xx} = y^2 H_0^{(1)}(\varrho) - (x^2 - y^2)H_1^{(1)}(\varrho) \qquad (10)$$

$$G_{yy} = -x^2 H_0^{(1)}(\varrho) + (x^2 - y^2)H_1^{(1)}(\varrho) \qquad (11)$$

$$G_{xy} = G_{yx} = 2xy H_1^{(1)}(\varrho) \quad \varrho = k_b|r - r'| \qquad (12)$$

Here, we consider a measurement setup where the antennas are placed parallel to the ϕ direction; hence only the ϕ component of the vector scattered field is measured. This scalar measurement can be expressed in terms of dyadic components:

$$G_{\phi x} = -G_{xx}\sin(\phi) + G_{xy}\cos(\phi) \qquad (13)$$

$$G_{\phi y} = -G_{yx}\sin(\phi) + G_{yy}\cos(\phi) \qquad (14)$$

Finally, the measured scattering field can be expressed as:

$$\Delta u_{TE}^{sct}(r) = k_b^2 \int_\Omega \delta\chi(r')G_{\phi x}(r;r')U_x^{inc}(r')d\Omega(r') \\ + k_b^2 \int_\Omega \delta\chi(r')G_{\phi y}(r;r')U_y^{inc}(r')d\Omega(r') \qquad (15)$$

where the incident field is defined as:

$$U_x^{inc}(r') = -\frac{(y - y')ik_b H_1^{(1)}(\varrho)}{4r} \qquad (16)$$

$$U_y^{inc}(r') = \frac{(x - x')ik_b H_1^{(1)}(\varrho)}{4r} \qquad (17)$$

Later, Eq. (15) can be converted into a system of linear equations as:

$$\Delta u_{TE}^{sct} = A_{TE}\delta\chi \qquad (18)$$

where A_{TE} is the transformation matrix for TE case illumination. In order to determine the differential contrast function for TE case, Tikhonov regularization can be used as in Eq. (7). Finally, the results obtained via TM and TE scattering schemes can be combined to construct the differential contrast function as:

$$\begin{bmatrix} A_{TM} \\ \frac{1}{\beta}A_{TE} \end{bmatrix} [\delta\chi] = \begin{bmatrix} \Delta u_{eTM}^{sct} \\ \Delta u_{eTE}^{sct} \end{bmatrix} \qquad (19)$$

where a constant β is chosen according to $\beta = \arg\min_{t \in \mathbb{C}} ||\delta\chi_{TE} - t\delta\chi_{TM}||^2$ in order to prevent one component (TE or TM) to become dominant in the solution.

2.3 Virtual prototype

In this section, to assess the feasibility of the proposed technique, we create a simulation model as shown in Fig. 1. Here, an anthropomorphically realistic head model, which is cropped from a full-body dielectric phantom (AustinMan) with 1-mm³ cubic voxels, is employed [37]. The head is surrounded by a half-wavelength circular dipole array with a radius of 12cm. The dipole antennas have an operating frequency of 900 MHz, and these antennas are immersed in a lossless coupling medium characterized by the relative dielectric constant of $\epsilon_r = 40$. This matching medium is employed to increase the penetration of the incident electromagnetic field into the interior parts of the brain. Moreover, by decreasing the wavelength, the matching medium enables to use of smaller antennas. Here, the designed antenna has a total length of 34 mm. As for the other dimensions, the radius of the metal arms is chosen as 0.3mm, and the length of the feeding gap between the two arms is 0.8mm. With these dimensions, the antennas can be placed vertically and horizontally, as shown in Fig. 1. Thirty-six of these antennas

Fig. 1 Simulation model
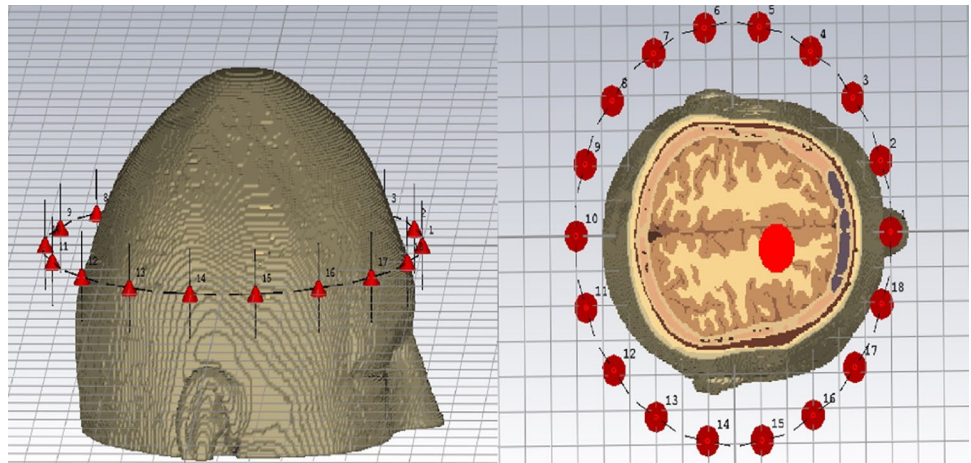
Table 1 Electrical properties of the Brain tissues

Tissue	ϵ_r	σ [S/m]	Tissue	ϵ_r	σ [S/m]
Blood	61.36	1.538	Blood Vessel	44.77	0.6961
Bone Corticai	12.45	0.1433	Bone Marrow	5.504	0.04021
Brain Gray Matter	52.73	0.9423	Brain White Matter	38.89	0.5908
Cerebellum	49.44	1.269	Cerebro Spinal Fluid	68.64	2.413
Dura	44.43	0.9611	Eye Sclera	55.27	1.167
Fat	5.462	0.05104	Muscle	55.03	0.9429
Skin Dry	41.41	0.8667	Tendon	45.83	0.7184
VitreousHumor	68.9	1.636			

(18 vertical for TM modes, 18 horizontal for TE modes) are placed to encircle the head model with equiangular separations as seen in Fig. 1, in order to excite both TM and TE modes with a single antenna array in the same measurement setup. For the TM case, the vertical antennas, which are perpendicular to the measurement plane, are fed through the gaps, while 18 horizontal dipoles act as passive metal elements with no feeding. For the TE case, the situation is reversed; that is, the vertical antennas are acting as passive metal objects, and the horizontal antennas, parallel to the measurement plane, are active and operating.

A hemorrhage is modeled by inserting spherical or elliptical inclusions (red region in Fig. 1) in each scenario. Dielectric permittivity and electric conductivity values of the tissues are given in Table 1 for the operating frequency of 900 MHz. As seen in Table 1, electrical properties such as relative permittivity and conductivity of the blood are significantly different from those of other brain tissues. Hence, it is possible to detect the hemorrhage-affected regions in the human brain by using electromagnetic waves at microwave frequencies. The AustinMan phantom provides these electrical parameters only for the operating frequency of 900 MHz,

and the operating frequency of 900 MHz appears to be an optimal choice for microwave-based brain stroke imaging [11, 13]. When the operating frequency is increased, highly conductive tissues (i.e., cerebrospinal fluid, vitreous humor, and gray matter) become too dominant, and differentiating these regions from the hemorrhage becomes difficult. On the other hand, decreasing the operating frequency negatively affects the resolution of reconstructed images. To be compatible with experimental systems, instead of electric field vectors, the scattering parameters at the antenna ports are calculated with a commercial electromagnetic simulator (CST) at the single operating frequency of $f = 900$ MHz for both TE and TM modes. The domain used in the forward problem simulation, which includes both the head model and the antennas, has $324 \times 305 \times 113 \approx 11 \times 10^6$ voxels. After obtaining scattering parameters from CST, these parameters are converted to the electric field by means of a calibration procedure. For this aim, a metallic cylinder with a radius of 5 cm, centered at the origin, is illuminated by line sources, and the scattering parameters for the same setup are simulated via CST. The scattered electric field for this calibration setup can be calculated via analytical formulas [39]. Then, the calibration coefficients are calculated by dividing the analytically calculated scattered electrical field by the corresponding scattering parameters for the same measurement point. Once these coefficients are obtained, the scattered electric field for any simulation setup can be calculated by multiplying the scattering parameters of that specific simulation with the previously obtained calibration coefficients.

3 Results

In this section, we present several numerical results to demonstrate the capabilities of the presented imaging formulation for ICH monitoring. The presented imaging formulation depends on linearization by Born approximation, and it is

well known that the retrieved electromagnetic properties under Born approximation are severely underestimated. However, the motivation of this study is to determine the geometrical extent of shrinking or growing ICH instead of retrieving the actual variation of electromagnetic properties of brain tissues. Hence, all the images are formed by normalizing the real, imaginary, or absolute values of retrieved differential contrast $\delta\chi$ for each point in the imaging domain for consecutive time steps ($t = 1, 2, ...$).

$$\mathcal{I}_t^{(re)} = \frac{Re(\delta\chi)}{\max(|Re(\delta\chi)|)} \tag{20}$$

$$\mathcal{I}_t^{(im)} = \frac{Im(\delta\chi)}{\max(|Im(\delta\chi)|)} \tag{21}$$

$$\mathcal{I}_t^{(abs)} = \frac{|\delta\chi|}{\max(|\delta\chi|)} \tag{22}$$

In all cases, the intracranial hematomas are positioned at $z = 0.75$cm plane, whereas the antenna array shown in Fig. 1 is centered at $z = 0$ plane. Besides, the simulated scattered electric fields are synthetically corrupted with additive white Gaussian noise for different signal-to-noise ratios of $SNR(dB) := 20\log_{10}|u^{sct}|/|n|$ where n denotes the noise term.

In the first scenario, a patient with a shrinking ICH is considered. For the first simulation, a spherical hematoma with a radius of 1.5cm is located at the point $(-3, 4)$ cm as shown in Fig. 2a. Then, the radius of the hematoma decreases to 1cm for the second simulation, as shown in Fig. 2b. The difference of both scattered fields Δu^s is used as the data of the inverse problem to construct the differential contrast function $\delta\chi$. Initially, the reconstructions of $\delta\chi$ for TE and TM modes are independently evaluated. The variation of normalized absolute value of the differential contrast function ($\mathcal{I}_1^{(abs)}$) obtained using A_{TM} and Δu_{TM}^{sct} is shown in Fig. 2c when the SNR is 80dB. The result suggests that the reconstructed image is reliable for detecting the locations of changes inside the brain. The variation of $\mathcal{I}^{(abs)}$ for TE mode, obtained from A_{TE} and Δu_{TE}^{sct} is shown in Fig. 2d. The result retrieved from the TE mode calculation has fewer artifacts and provides a better visual representation for the same noise level compared to the TM case. In fact, it is possible to improve both reconstructions by increasing the number of antennas. However, it is highly preferable to reduce the number of antennas around the brain for the patients' comfort. To take advantage of both TE and TM polarizations, the reconstructions are repeated by using Eq. (19), and the retrieved result is shown in Fig. 2e. It is clear that while both schemes are capable of detecting and locating the change, which is the shrinking ICH inside the brain phantom, it is advantageous to combine the different

polarizations to obtain a better imaging quality. Thus, the latter results are demonstrated only for the combined TM-TE algorithm. Whereas the geometrical extends of the ICH can be determined by observing $\mathcal{I}^{(abs)}$, it is not possible to detect the type of changes (growing or shrinking regions) from an image formed by taking the absolute value of $\delta\chi$. The images generated by the normalized real and imaginary parts of the reconstructed $\delta\chi$ are shown in Fig. 2f and g, respectively. Regions with values around -1 in $\mathcal{I}^{(re)}$ indicate the shrinking of the ICH, whereas the variation in $\mathcal{I}_1^{(im)}$ is cluttered to identify the type of change.

In the second scenario, a growing ICH is considered. Initially, an elliptic hematoma, with radii of 0.5cm and 0.71cm, is centered at (0.75, -0.75)cm for the first simulation as shown in Fig. 3a. Then, for the second simulation, the radii of the hematoma increase to 0.75cm for both axes, as shown in Fig. 3b. The retrieved images of $\mathcal{I}_1^{(abs)}$ and $\mathcal{I}_1^{(re)}$ are shown in Fig. 3d and e, respectively. This time, the region with values around 1 in $\mathcal{I}_1^{(re)}$ (Fig. 3e) indicates that the ICH is growing in size. These results demonstrate that $\mathcal{I}^{(abs)}$ indicates the location of the changes, while $\mathcal{I}^{(re)}$ shows the nature of the evolutions for both growing and shrinking scenarios. In order to eliminate the artifacts, an indicator image can be constructed as:

$$\mathcal{I}_t^{(ind)} = \mathrm{sgn}(Re(\delta\chi_t))u(|Re(\delta\chi_t)| - T_0);$$
$$T_0 = 0.5\max(|\delta\chi_0|) \tag{23}$$

where $u(\cdot)$ is the unit step function, $\delta\chi_t$ is the differential contrast at t^{th} time step and T_0 is the threshold obtained from the very first differential contrast of $\delta\chi_0$. The indicator images reconstructed with the combined approach for this scenario are depicted in Fig. 3f. At subsequent measurement, the radius of the hematoma further increases to 1cm, as shown in Fig. 3f. The variation of $\mathcal{I}_2^{(abs)}$ and $\mathcal{I}_2^{(re)}$, which are plotted in Fig. 3g and h, further confirms that the ICH is still growing. With these approaches, it is possible to monitor the volumetric changes of hematoma as shown in Fig. 3i. In the last simulation, the ICH region remains the same. In this state; the reconstructed $\mathcal{I}_3^{(abs)}$ and $\mathcal{I}_3^{(re)}$, which are plotted in Fig. 3j and k, are randomly changing, which implies that the only difference between the two fields at consecutive time steps is due to the noise. The indicator image $\mathcal{I}_3^{(ind)}$ of this state, which is shown in Fig. 3l, clearly shows that there is no change for ICH.

To further test the presented indicator, a case with multiple ICH region evolutions is considered. Initially, a hemorrhagic region with a radius of 1 cm, centered at the point $(-3, 4)$cm, is assumed to be present for the first simulation as seen in Fig. 2a. Later, this hematoma shrinks, and another hematoma with a radius of $1.5cm$, centered at the point $(4, -4)$cm, occurs for the second simulation as seen in Fig. 4a. The reconstructed images by plotting $\mathcal{I}_1^{(abs)}$ and
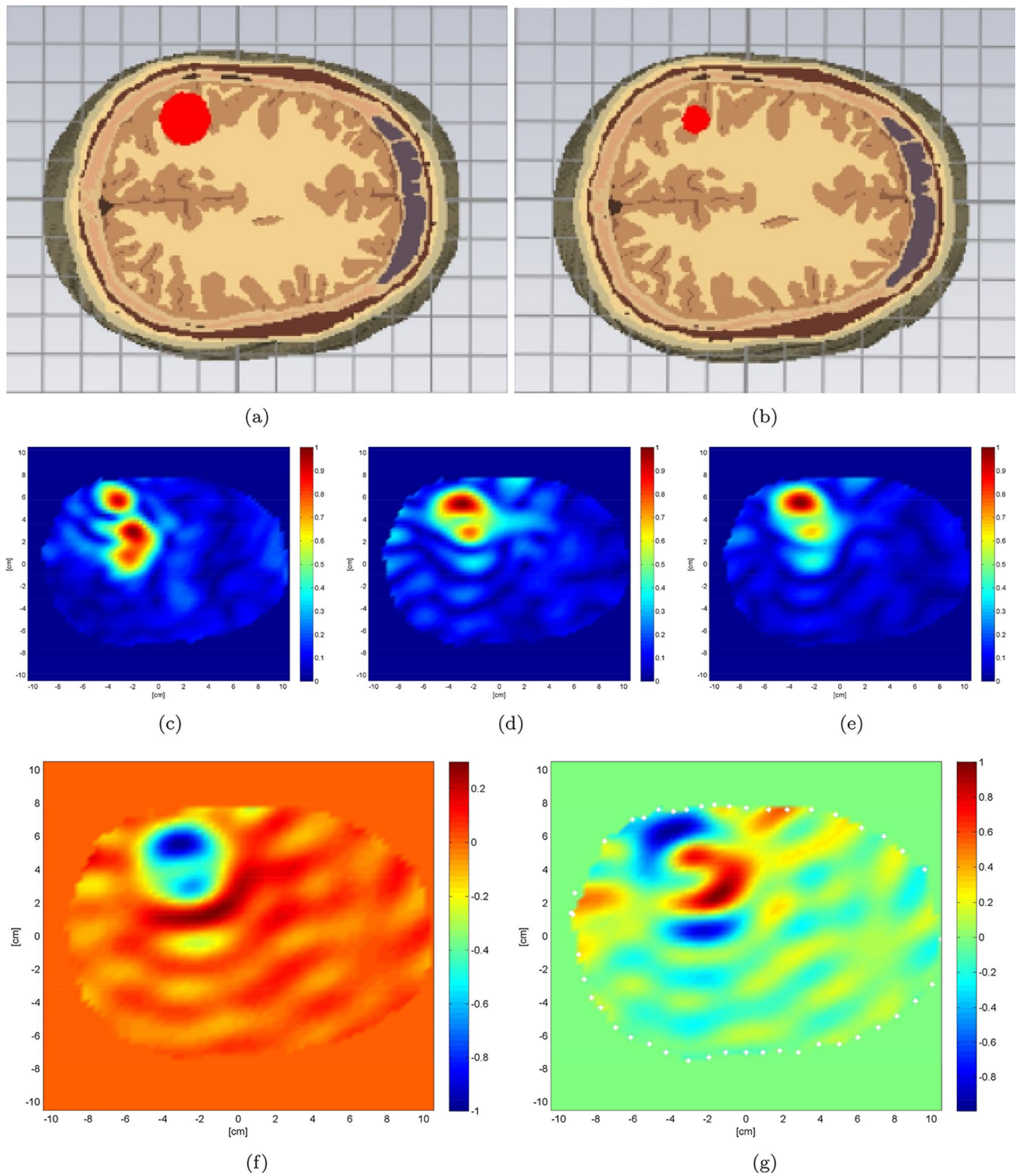
Fig. 2 Dielectric head phantom for shrinking ICH scenario: The simulation model (**a**) for the first time step, and (**b**) for the second time step. Reconstructed normalized images: (**c**) $\mathcal{I}_1^{(abs)}$ for TM polarization, (**d**) $\mathcal{I}_1^{(abs)}$ for TE polarization, (**e**) $\mathcal{I}_1^{(abs)}$ when TM and TE polarization are used together, (**f**) $\mathcal{I}_1^{(re)}$ when TM and TE polarization are used together, (**g**) $\mathcal{I}_1^{(im)}$ when TM and TE polarization are used together (the SNR is 80dB for all cases)
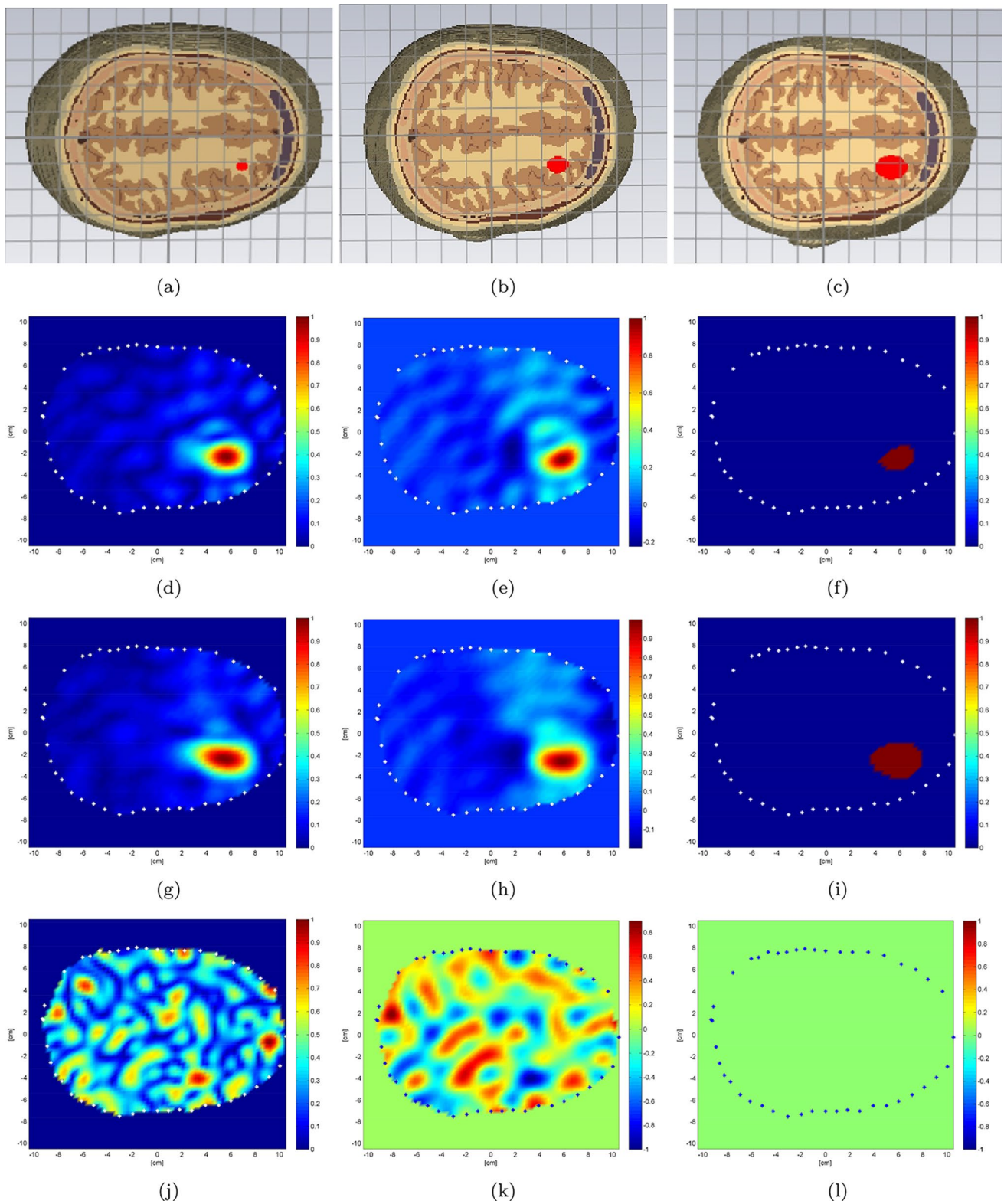
Fig. 3 Dielectric head phantom for growing ICH scenario: The simulation model (**a**) for the first time step, (**b**) for the second time step, and (**c**) for the third time step. Reconstructed normalized images: (**d**) $\mathcal{I}_1^{(abs)}$, (**e**) $\mathcal{I}_1^{(re)}$, (**f**) $\mathcal{I}_1^{(ind)}$, (**g**) $\mathcal{I}_2^{(abs)}$, (**h**) $\mathcal{I}_2^{(re)}$, (**i**) $\mathcal{I}_2^{(ind)}$, (**j**) $\mathcal{I}_3^{(abs)}$, (**k**) $\mathcal{I}_3^{(re)}$, (**l**) $\mathcal{I}_3^{(ind)}$, when the SNR is 80dB for all cases

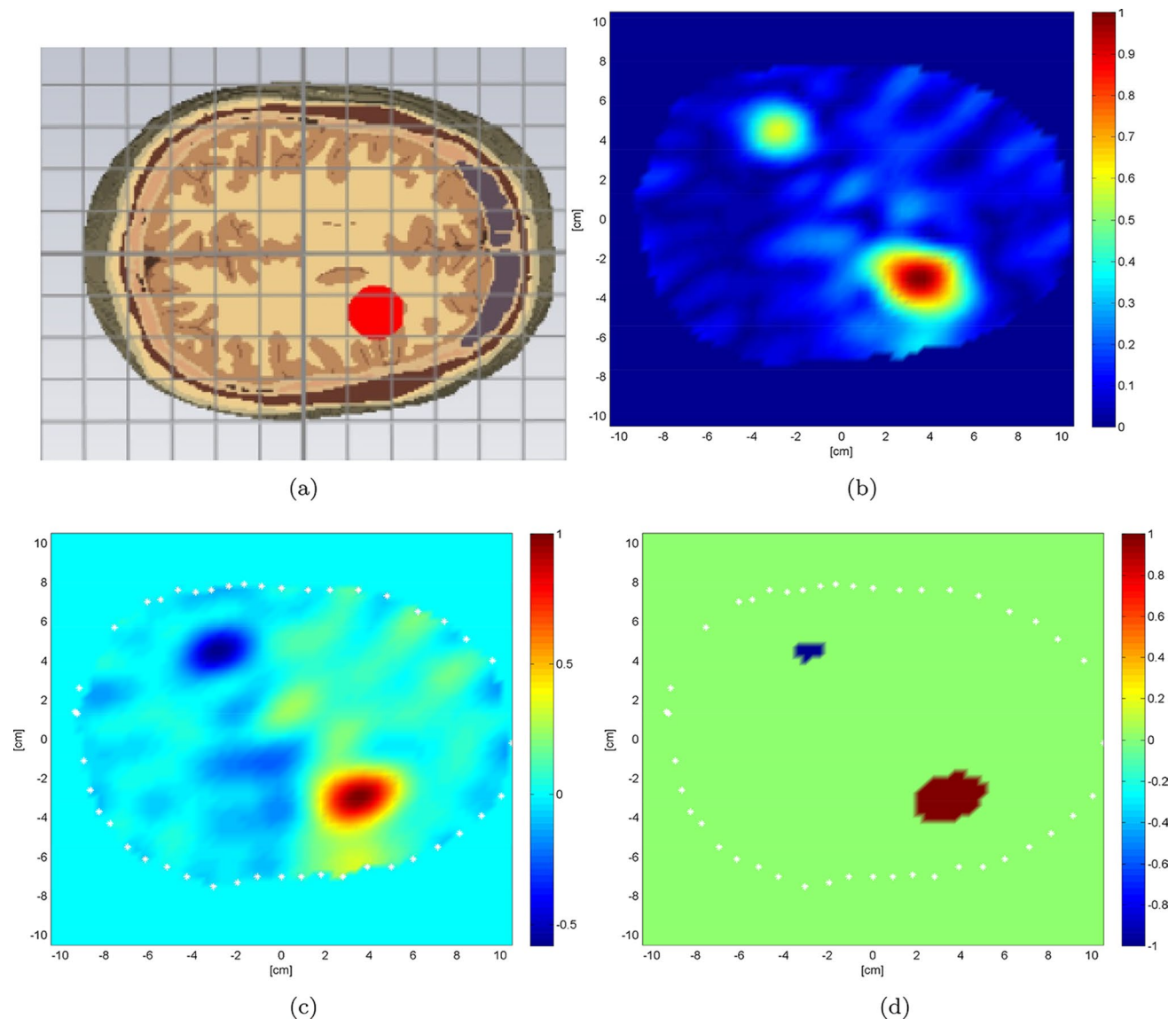**Fig. 4** (**a**) Dielectric head phantom for the second simulation when the first simulation is performed for the case depicted in Fig. 2a. Reconstructed normalized images: (**b**) $\mathcal{I}_1^{(abs)}$, (c) $\mathcal{I}_1^{(re)}$, (d) $\mathcal{I}_1^{(ind)}$ when the SNR is 80dB

$\mathcal{I}_1^{(re)}$ are shown in Fig. 4b and c. The volumetric change for the growing region is greater than the shrinking hematoma hence the regions associated with growing ICH have a larger spot in both images. Later, the indicator image, which is shown in Fig. 4d, identifies both the shrinking and the growing hematomas.

In order to determine the robustness and repeatability of the presented method, a new scenario is considered. Here, for assessing the proposed algorithm with a quantitative criterion, the indicator images that are obtained by Eq. (23) are compared against the exact images in terms of an error term

$$
\text{err}\% := \frac{100}{N} \sum_p |\mathcal{I}(p) - \mathcal{I}^x(p)| \tag{24}
$$

where N is the total number of pixels, $\mathcal{I}(p)$ and $\mathcal{I}^x(p)$ denote the pixel values of the reconstructed and the exact image. In this scenario, at the first simulation, a scattered field from a healthy brain phantom is collected. Then a spherical hematoma with a radius of 0.5cm, centered at the point $(-3, 4)$cm, is assumed to be present for the second simulation as seen in Fig. 3a. Later, a Monte Carlo analysis is performed where the reconstruction procedure is repeated 100 times for different signal-to-noise ratios (SNR) of 10dB to 80dB. The variation
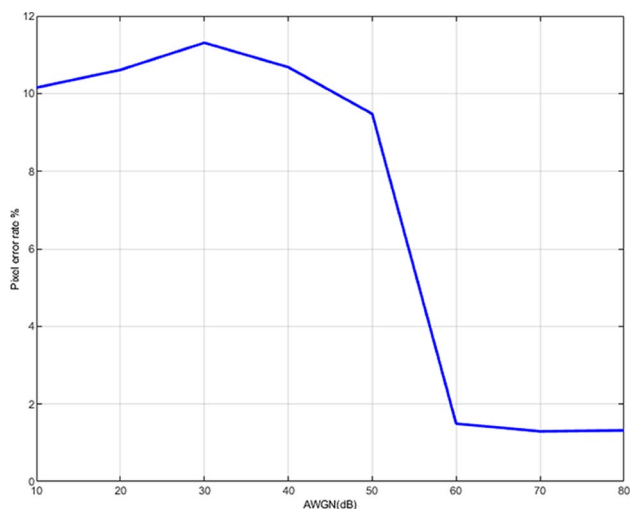
Fig. 5 Percentage error rate

of the percentage error rate in Eq. (24) is shown in Fig. 5. This result signifies that the presented method is stable, provided that the noise on the scattered field is below a certain limit. As a whole, the presented numerical results demonstrate that the presented method is capable of detecting the geometrical extend and volumetric evolution of an ICH.

4 Discussion

ICH is a critical condition with a high degree of mortality; hence any new technology that aims at ICH patients is important and challenging. Here, we present a linear microwave imaging technique that aims to address the continuous monitoring of the volumetric evolution of ICH. Whereas the capabilities of the presented technique are demonstrated with several simulations, it is clear that there are open questions on the presented technique as well as on the usage of microwave imaging for the brain in general.

The presented virtual prototype describes the antennas and the antenna placement with the assumption of an impedance matching medium into which the antennas are embedded. However, the realization of an impedance matching medium that is in contact with the head is an open question. One possible approach is embedding the antennas into solid dielectrics that are touching the head, as demonstrated in [30]. However, the risks associated with being in direct contact with the head of an ICH patient are not clear.

The presented results with the method are all reconstructed from scattering parameters (instead of the actual electric field), which can be accurately measured with commercially available vector network analyzers (VNA). However, experimental verification of the presented method with a tissue-mimicking brain phantom is an open question due to the lack of the impedance matching medium. However, even with dielectric phantoms, it is largely an open question how accurately a tissue-mimicking brain phantom can represent the actual brain with ICH conditions. In that sense, a numerical dielectric phantom that is derived from a high-resolution MRI model [37] may still be a better option to understand the performance of a microwave imaging technique.

Another open question is the possible adverse effect of microwave usage for continuous monitoring of ICH. In the case of an experimental prototype based on the presented method, microwave measurements are performed in terms of scattering parameters with a VNA. For a typical VNA, the output power is generally limited to 10mW (or lower). Furthermore, by using dipole antennas, the effective isotropic radiated power (EIRP) can be much lower as compared to mobile communication standards. Nevertheless, the possible adverse effects of continuous monitoring of ICH with microwave is a multi-disciplinary open question.

Consequently, even with its open questions, the presented research is an important step toward addressing a global healthcare issue.

5 Conclusions

This paper investigated the feasibility of continuous monitoring of ICH via a linear microwave inversion technique. In particular, we present a differential imaging technique that reconstructs single-slice images of the brain by taking advantage of both TM and TE polarizations. In order to assess the performance of the method, different scenarios are numerically investigated using a 3D dielectric head phantom. The computational analysis signifies that the presented technique accurately determines the geometrical extends and the type of volumetric evolutions of hematomas inside the cranium. Furthermore, the repeatability analysis demonstrates the robustness of the procedure under noisy conditions.

References

1. Carhuapoma JR, Mayer SA, Hanley DF (eds) (2009) Intracerebral hemorrhage. Cambridge University Press, Cambridge
2. Candefjord S, Winges J, Malik AA, Yu Y, Rylander T, McKelvey T, Fhager A, Elam M, Persson M (2017) Microwave technology for detecting traumatic intracranial bleedings: tests on phantom of subdural hematoma and numerical simulations. Med Biol Eng Compu 55(8):1177–1188
3. Caorsi S, Frattoni A, Gragnani GL, Nortino E, Pastorino M (1991) Numerical algorithm for dielectric-permittivity microwave imaging of inhomogeneous biological bodies. Med Biol Eng Compu 29(6):NS37–NS44

4. Chandra R, Zhou H, Balasingham I, Narayanan RM (2015) On the opportunities and challenges in microwave medical sensing and imaging. IEEE Trans Biomed Eng 62(7):1667–1682

5. Fajardo JE, Lotto FP, Vericat F, Carlevaro CM, Irastorza RM (2020) Microwave tomography with phaseless data on the calcaneus by means of artificial neural networks. Med Biol Eng Compu 58(2):433–442

6. Shao W, McCollough T (2020) Advances in microwave near-field imaging: Prototypes, systems, and applications. IEEE Microw Mag 21(5):94–119

7. Song H, Li Y, Men A (2018) Microwave breast cancer detection using time-frequency representations. Med Biol Eng Compu 56(4):571–582

8. Arıcı EK, Yapar A (2019) An inverse scattering approach based on inhomogeneous medium green's functions for microwave imaging of brain strokes. Adv Electromagn 8(2):53–58

9. Munawar Qureshi A, Mustansar Z, Mustafa S (2018) Finite-element analysis of microwave scattering from a three-dimensional human head model for brain stroke detection. R Soc Open Sci 5(7):180319

10. Bisio I, Fedeli A, Lavagetto F, Pastorino M, Randazzo A, Sciarrone A, Tavanti E (2018) A numerical study concerning brain stroke detection by microwave imaging systems. Multimed Tools Appl 77(8):9341–9363

11. Bisio I, Estatico C, Fedeli A, Lavagetto F, Pastorino M, Randazzo A, Sciarrone A (2020) Variable-exponent lebesgue-space inversion for brain stroke microwave imaging. IEEE Trans Microw Theory Tech 68(5):1882–1895

12. Coli VL, Tournier P-H, Dolean V, El Kanfoud I, Pichot C, Migliaccio C, Blanc-Féraud L (2019) Detection of simulated brain strokes using microwave tomography. IEEE J Electromagn RF Microw Med Biology 3(4):254–260

13. Dilman İ, Yıldırım U, Coşğun S, Doğu S, Çayören M, Akduman I (2016) Feasibility of brain stroke imaging with microwaves. In: 2016 IEEE Asia-pacific conference on applied electromagnetics (APACE). IEEE, pp 334–338

14. Dilman İ, Akıncı MN, Çayören M, Akduman İ (2017) Differential microwave imaging of the stroke-affected brain via diffraction tomography. In: 2017 25th Telecommunication forum (TELFOR). IEEE, pp 1–4

15. Dilman I, Bilgin E, Cosgun S, Cayoren M, Akduman I (2018) A compressive sensing application on microwave diffraction tomography for the microwave imaging of a stroke affected human brain. In: 2018 IEEE MTT-S International Conference on Numerical Electromagnetic and Multiphysics Modeling and Optimization (NEMO). pp 1–4

16. Fedeli A, Schenone V, Randazzo A, Pastorino M, Henriksson T, Semenov S (2021) Nonlinear s-parameters inversion for stroke imaging. IEEE Trans Microw Theory Tech 69(3):1760–1771

17. Sohani B, Khalesi B, Ghavami N, Ghavami M, Dudley S, Rahmani A, Tiberi G (2020) Detection of haemorrhagic stroke in simulation and realistic 3-d human head phantom using microwave imaging. Biomed Signal Process Control 61:102001

18. Tournier P-H, Bonazzoli M, Dolean V, Rapetti F, Hecht F, Nataf F, Aliferis I, El Kanfoud I, Migliaccio C, De Buhan M et al (2017) Numerical modeling and high-speed parallel computing: New perspectives on tomographic microwave imaging for brain stroke detection and monitoring. IEEE Antennas Propag Mag 59(5):98–110

19. Wang L (2020) Multifrequency microwave imaging for brain stroke detection. Mol Cell Biomech 17(1):33

20. Yıldırım U, Dilman İ, Bilgin E, Doğu S, Çayören M, Akduman İ (2017) Continuous monitoring of hemorrhagic brain strokes via contrast source inversion. In: 2017 11th European conference on antennas and propagation (EUCAP). IEEE, pp 408–411

21. Bashri MSR, Arslan T (2018) Low-cost and compact rf switching system for wearable microwave head imaging with performance verification on artificial head phantom. IET Microwaves, Antennas Propagation 12(5):706–711

22. Çayören M, Akduman İ (2018) Emerging Electromagnetic Technologies for Brain Diseases Diagnostic, Monitoring and Therapy, chapter Continuous Monitoring of Hemorrhagic Strokes via Differential Microwave Imaging. Springer, Cham, pp ages 37–57

23. Karadima O, Rahman M, Sotiriou I, Ghavami N, Lu P, Ahsan S, Kosmas P (2020) Experimental validation of microwave tomography with the dbim-twist algorithm for brain stroke detection and classification. Sensors 20(3):840

24. Merunka I, Massa A, Vrba D, Fiser O, Salucci M, Vrba J (2019) Microwave tomography system for methodical testing of human brain stroke detection approaches. International Journal of Antennas and Propagation 2019

25. Mobashsher AT, Mahmoud A, Abbosh AM (2016) Portable wideband microwave imaging system for intracranial hemorrhage detection using improved back-projection algorithm with model of effective head permittivity. Sci Rep 6:20459

26. Mohammed BJ, Abbosh AM, Mustafa S, Ireland D (2014) Microwave system for head imaging. IEEE Trans Instrum Meas 63(1):117–123

27. Tobon Vasquez JA, Scapaticci R, Turvani G, Bellizzi G, Rodriguez-Duarte DO, Joachimowicz N, Duchêne B, Tedeschi E, Casu MR, Crocco L et al (2020) A prototype microwave system for 3d brain stroke imaging. Sensors 20(9):2607

28. Ljungqvist J, Candefjord S, Persson M, Jönsson L, Skoglund T, Elam M (2017) Clinical evaluation of a microwave-based device for detection of traumatic intracranial hemorrhage. J Neurotrauma 34(13):2176–2182

29. Scapaticci R, Bucci OM, Catapano I, Crocco L (2014) Differential microwave imaging for brain stroke followup. International Journal of Antennas and Propagation, 2014

30. Persson M, Fhager A, Trefna HD, Yu Y, McKelvey T, Pegenius G, Karlsson J-E, Elam M (2014) Microwave-based stroke diagnosis making global prehospital thrombolytic treatment possible. IEEE Trans Biomed Eng 61(11):2806–2817

31. Amineh RK, Ravan M, Trehan A, Nikolova NK (2011) Near-field microwave imaging based on aperture raster scanning with tem horn antennas. IEEE Trans Antennas Propag 59(3):928–940

32. Devaney AJ (1982) A filtered backpropagation algorithm for diffraction tomography. Ultrason Imaging 4(4):336–350

33. Doğu S, Akıncı MN, Çayören M, Akduman İ (2019) Truncated singular value decomposition for through-the-wall microwave imaging application. IET Microwaves, Antennas & Propagation 14(4):260–267

34. Doğu S, Akinci MN, Gose E (2020) Experimental moving target imaging in a nonanechoic environment with linear sampling method. IEEE Geoscience and Remote Sensing Letters

35. Soldovieri F, Solimene R (2007) Through-wall imaging via a linear inverse scattering algorithm. IEEE Geosci Remote Sens Lett 4(4):513–517

36. Soldovieri F, Brancaccio A, Prisco G, Leone G, Pierri R (2008) A kirchhoff-based shape reconstruction algorithm for the multi-monostatic configuration: The realistic case of buried pipes. IEEE Trans Geosci Remote Sens 46(10):3031–3038

37. Massey JW, Yilmaz AE (2016) Austinman and austinwoman: High-fidelity, anatomical voxel models developed from the vhp color images. In: 38th Annual International Conference of the IEEE Engineering in Medicine and Biology Society (EMBC). IEEE, pp 3346–3349

38. Colton D, Kress R (2013) Inverse acoustic and electromagnetic scattering theory. Springer, New York

39. Balanis CA (2012) Advanced engineering electromagnetics. John Wiley & Sons, Hoboken

İsmail Dilman received the B.S. degree from the Department of Electronics and Telecommunication Engineering, Yildiz Technical University, Istanbul, Turkey, in 2009, and the M.S. degree from the Program of Telecommunication Engineering, Istanbul Technical University, Istanbul, in 2016, where he is currently pursuing the Ph.D. degree. His research interests include microwave imaging, microwave dielectric spectroscopy, and inverse scattering problems.

Egemen Bilgin was born in Istanbul, Turkey, in 1984. He received the B.Sc., M.Sc., and Ph.D. degrees in electronics and communication engineering from Istanbul Technical University, Maslak, Turkey, in 2008, 2010, and 2016 respectively. He is currently a Faculty Member of the Electrical and Electronics Engineering Department, MEF University, Maslak. His research interests include electromagnetic and acoustic scattering, integral equations, and inverse scattering problems

Mehmet Nuri Akıncı was born in Ankara, Turkey, in 1992. He received the B.Sc. (Hons.) and Ph.D. degrees in electronics and communication engineering from Istanbul Technical University, Istanbul, Turkey, in 2013 and 2017, respectively. He was a Visiting Scientist with the Institute for Electromagnetic Sensing of the Environment, National Research Council of Italy, Naples, Italy, in 2015, and Virginia Commonwealth University, Richmond, VA, USA, in 2016. He is currently an Assistant Professor with the Department of Electronics and Communication Engineering, Istanbul Technical University. His current research interests include inverse scattering problems, microwave measurement systems, and optics.

Sema Coşğun received the B.Sc. and M.Sc. degrees in electrical and electronics engineering from Ataturk University, Erzurum, Turkey, in 2012 and 2015, respectively, and the Ph.D. degree in electronics and communication engineering from Istanbul Technical University, Istanbul, Turkey, in 2020. She is currently a Faculty Member of the Electrical and Electronics Engineering Department, Bolu Abant Izzet Baysal University, Bolu, Turkey. Her research focuses on biomedical applications of microwave imaging and machine learning in electromagnetics.

Semih Doğu received the B.Sc. degree in electrical engineering and electronics and communication engineering from Yildiz Technical University, Istanbul, Turkey, in 2015 and 2016 respectively, and the M.Sc. degree in telecommunication engineering from Istanbul Technical University, Istanbul, Turkey, in 2017. He is currently pursuing the Ph.D. degree in telecommunication engineering at Istanbul Technical University, Istanbul, Turkey. He is currently a Research and Teaching Assistant with the Department of Electronics and Communication Engineering, Istanbul Technical University, Istanbul, Turkey. From 2021 to 2022, he was a visiting researcher in electrical engineering at McMaster University, Hamilton, ON, Canada. His current research interests include electromagnetic scattering problems, imaging methods for noninvasive diagnostics, through-the-wall radar, and biomedical imaging. He was a recipient of the 2016 IEEE Antennas and Propagation Ulrich L. Rohde Innovative Conference Paper Award on Antenna Measurements and Applications.

Mehmet Çayören received the B.Sc. degree in electrical and electronics engineering from Istanbul University, Istanbul, Turkey, in 2001, and the M.Sc. and Ph.D. degrees in electronics and communication engineering from Istanbul Technical University, Istanbul, in 2004 and 2009, respectively. From 2008 to 2009, he was a Visiting Scholar with the Department of Mathematical Sciences, University of Delaware, Newark, DE, USA. He is currently a Professor of electronics and communication engineering with Istanbul Technical University. His research interests include microwave imaging, inverse scattering, and computational electromagnetics.

İbrahim Akduman was born in Konya, Turkey, in 1963. He received the B.Sc., M.S., and Ph.D. degrees in electronics and communication engineering from Istanbul Technical University, Istanbul, Turkey, in 1984, 1987, and 1990, respectively. He was a Visiting Scientist with the Tandon School of Engineering, New York University, Brooklyn, NY, USA, in 1991; King's College London, London, UK, in 1995; the New Jersey Institute of Technology, Newark, NJ, USA, in 2000; and the University of Göttingen, Göttingen, Germany, in 2001. He was the Dean of the Electrical and Electronics Engineering Faculty, Istanbul Technical University, from 1999 to 2001, and the Vice President from 2002 to 2004, where he is currently a Full Professor and the Head of the Electromagnetic Research Group. He is also a shareholder of a company, where he is involved in research and developing products for medical application of electromagnetic fields. His current research interests include microwave tomography and electromagnetics in medicine. Prof. Akduman received the Turkish Scientific and Technological Research Council Young Scientist Award in 2000.